ROYAL SOCIETY OPEN SCIENCE

rsos.royalsocietypublishing.org

Research

Cite this article: Thummavichai K, Wang N, Xu F, Rance G, Xia Y, Zhu Y. 2018 *In situ* investigations of the phase change behaviour of tungsten oxide nanostructures. *R. Soc. open sci.* **5**: 171932.
http://dx.doi.org/10.1098/rsos.171932

Received: 17 November 2017
Accepted: 20 March 2018

Subject Category:
Chemistry

Subject Areas:
materials science/inorganic chemistry

Keywords:
phase transition, tungsten oxide, nanowires

Author for correspondence:
Yanqiu Zhu
e-mail: y.zhu@exeter.ac.uk

This article has been edited by the Royal Society of Chemistry, including the commissioning, peer review process and editorial aspects up to the point of acceptance.

THE ROYAL SOCIETY PUBLISHING

In situ investigations of the phase change behaviour of tungsten oxide nanostructures

Kunyapat Thummavichai[1], Nannan Wang[1], Fang Xu[2], Graham Rance[3], Yongda Xia[2] and Yanqiu Zhu[1]

[1]College of Engineering Mathematics and Physical Sciences, University of Exeter, Exeter EX4 4QF, UK
[2]Faculty of Engineering, and [3]Nanoscale and Microscale Research Centre, University of Nottingham, Nottingham NG7 2RD, UK

YZ, 0000-0003-3659-5643

This study uses two *in situ* techniques to investigate the geometry and phase change behaviour of bundled ultrathin $W_{18}O_{49}$ nanowires and WO_3 nanoparticles. The *in situ* X-ray diffraction (XRD) results have shown that the phase transition of WO_3 nanoparticles occurs in sequence from monoclinic (room temperature) → orthorhombic (350°C) → tetragonal (800°C), akin to bulk WO_3; however, $W_{18}O_{49}$ nanowires remain stable as the monoclinic phase up to 500°C, after which a complete oxidation to WO_3 and transformation to the orthorhombic β-phase at 550°C is observed. The *in situ* Raman spectroscopy investigations have revealed the Raman peak downshifts as the temperature increases, and have identified the 187.6 cm^{-1} as the fingerprint band for the phase transition from γ- to β-phase of the WO_3 nanoparticle. Furthermore, WO_3 nanoparticles exhibit the γ- to β-phase conversion at 275°C, which is about 75°C lower than the relaxation temperature of 350°C for the monoclinic γ-$W_{18}O_{49}$ nanowires. These new fundamental understandings on the phase transition behaviour offer important guidance for the design and development of tungsten oxide-based nanodevices by defining their allowed operating conditions.

1. Introduction

Tungsten oxides are one of the most promising transition metal oxide semiconducting materials which possess outstanding electronic, optical, chromic and sensing properties that make them suitable for a diverse range of energy-related applications [1–4]. Tungsten oxides have various interesting structural

transformations, in addition to their numerous non-stoichiometric chemical compositions, hence they have attracted immense research attention. For decades, studies have been carried out to explore their different sub-stoichiometric structures and phase transformation characteristics, attempting to establish structure–property relationships and thus guide the suitability for a multitude of advanced applications, such as in solar cells, displays, microelectronic, superconductivity, photocatalytic and especially smart optical devices [1,5–8]. Bulk tungsten trioxide (WO_3) exhibits a ReO_3-type cubic structure (perovskite-like structure), with corner-sharing WO_6 octahedral as the basic structure element, while bulk monoclinic $W_{18}O_{49}$ (i.e. $WO_{2.72}$), a typical stable form of sub-stoichiometric oxide, consists of an ordered two-dimensional lattice of edge-sharing WO_6 octahedral forming a network of pentagonal columns interspersed with hexagonal channels [9]. Under ambient pressure, the phase changes of bulk WO_3 are temperature dependent, exhibiting a clear sequence of phase transitions with elevating temperature: from monoclinic II (ε-WO_3, less than −43°C) to triclinic (δ-WO_3, −43 to 17°C), to monoclinic I (γ-WO_3, 17–330°C), to orthorhombic (β-WO_3, 330–740°C) and, finally, to tetragonal (α-WO_3, greater than 740°C) [10,11]. Bulk $W_{18}O_{49}$ essentially follows an analogous pattern of phase transition.

Recent developments in nanostructured materials present new opportunities and challenges for research and applications, with nanorods and nanowires of tungsten oxides convincingly outperforming their traditional bulk counterparts in the applications described previously [2,3,12,13]. However, an in-depth understanding of the phase transition characteristics of these new nanostructures has yet to be achieved, which will ultimately restrict the development of new technologies based on these novel nanomaterials. As a typically stable form of nanostructured tungsten oxide, $W_{18}O_{49}$ nanorods and nanowires have most often been reported and have stood out from other sub-stoichiometric compositions since their first synthesis a decade ago [14]. Therefore, using advanced techniques to investigate the fundamental structural features of this type of one-dimensional nanomaterial is particularly of interest.

Nanorods and nanowires of $W_{18}O_{49}$, akin to their bulk crystalline form, consist of a similar WO_6 octahedral structure, hence could possess a variety of complex phase transitions and a temperature- and pressure-dependent phase transition sequence. Owing to the complex nature of tungsten oxides, several approaches using conventional techniques have been attempted to investigate, understand and explain the characteristics of their phase transformations. Chen *et al*. [15] studied the phase transition of WO_3 nanowires under different hydrostatic pressure conditions, ranging from atmospheric to 42.5 GPa. Their Raman spectra have confirmed that the WO_3 nanowires have higher phase transition pressures than their corresponding bulk WO_3 nanocrystals. Cazzanelli [16], using both X-ray diffraction (XRD) and Raman spectroscopy to study WO_3 and H-doped WO_3 spherical powders, has shown that a sequence of phase transitions, from monoclinic to orthorhombic to tetragonal, has been achieved with increasing temperatures from room temperature up to 800°C. Raman spectroscopy is a more effective technique than XRD in revealing structure transitions of the complex WO_x system, as Raman spectroscopy has higher sensitivity to changes in the positions of and bonding between the W and O atoms in the crystal lattice, while with XRD it is often difficult to distinguish the similar and often overlapping diffraction peaks. Using Raman spectroscopy, Lai [17] has investigated the structural change of WO_3 nanoplatelet films containing different amounts of ammonium fluoride and related it to the photocatalytic properties. Lu *et al*. [18] have reported the oxidation and phase transition of sub-stoichiometric $W_{18}O_{49}$ nanowires using intrinsic Raman spectroscopy by changing the input laser power.

The understanding of the fundamental aspects of the phase transformations of these nanostructured WO_x materials could unlock the mechanisms of these phase transitions, distinguish the difference between the nano and bulk forms and provide effective guidance towards the design and development of new devices. For example, the application of WO_x as the detecting element in electrochemical gas sensors normally involves the use of a high operating temperature to compensate for the negative effect of baseline drifting. As semiconducting materials aimed at nano-device applications, severe changes in temperature and pressure could lead to unexpected unstable performance and even failure, due to undesired phase transitions. In this paper, we report our investigations into the reversibility of the relationship between temperature and phase transition behaviour of ultrathin $W_{18}O_{49}$ nanowires, relative to spherical WO_3 nanoparticles, by using two *in situ* hot-stage techniques, namely XRD and Raman spectroscopy, combined with *ex situ* electron microscopy analyses. This fundamental study offers the potential for phase and morphology control via temperature under different atmosphere conditions, as we believe that the temperature-associated phase and morphology changes could affect the structure transitions by way of lattice distortion, relaxation of the W–O bonding and oxygen vacancy inside the WO_x structures. These impacts would, therefore, influence the final performance of the nanomaterials in

chromic device and sensor applications. We hope this study could serve as an important guidance for the design and optimization of future WO_x-based devices where temperature is involved during operation.

2. Material and characterizations

$W_{18}O_{49}$ nanowires, approximately 2–5 nm in diameter and up to 2 µm in length, were prepared by a simple solvothermal technique by reacting WCl_6 with cyclohexanol at 200°C for 6 h, as previously described in detail [19–21]. WO_3 nanoparticles, approximately 40 nm in diameter, were purchased from Sigma Aldrich (UK). Both the as-purchased WO_3 nanoparticles and the as-prepared $W_{18}O_{49}$ nanowire thin films were prepared as follows: 0.1 g dry powder was dispersed in 2 ml ethanol, which was then dispersed in an ultrasonic bath for 30 min at room temperature. After forming a homogeneous suspension, 0.6 ml of this suspension was dropcast onto a quartz substrate to form a thin film, which was then dried under room temperature overnight, prior to the *in situ* hot-stage XRD (D8 advanced) investigation, using a Cu radiation generated at 40 kV and 40 mA. The measurements were recorded in 50°C intervals, from room temperature up to 900°C under low vacuum condition. The heating rate was 50°C min^{-1}, with 10 min dwell time for each step to record the diffraction profile. The scanned 2θ range was 20–40° for the WO_3 and 20–45° for the $W_{18}O_{49}$ samples. The data were collected and processed using DIFFRAC.SUITE (Bruker axs 2009–2016, v.6.5.0) and DIFFRAC.EVA (Bruker axs 2010–2016, v. 4.2.0.31), respectively. The dimensional and morphological changes of the post-treated WO_3 and $W_{18}O_{49}$ nanostructures at selected stages were observed using a HITACHI S3200N scanning electron microscope (SEM), operated at 20 kV. The JEM-1400 transmission electron microscope (TEM) operated at 200 kV was used to investigate the HRTEM and SAED image of each sample. X-ray photoelectron spectroscopy (XPS) was used to determine the different chemical compositions between WO_3 and $W_{18}O_{49}$. The XPS study was operated via a Kratos AXIS ULTRA spectrometer with a monochromated Al KR X-ray source (1486.6 eV) which was operated at a 15 kV anode potential and a 10 mA emission current. The XPS data were collected and analysed using SPECTRA, v. 8.5-D-A and Casa XPS, v. 2.3.16 PR 1.6, respectively. Raman spectroscopy was conducted using a Horiba–Jobin–Yvon LabRAM HR spectrometer. Spectra were acquired using a 532 nm laser at variable power (0.01–100%, 0.00336–33.6 mW), a 50× objective and a 300 µm confocal pinhole. To simultaneously scan a range of Raman shifts, a 600 lines mm^{-1} rotatable diffraction grating along a path length of 800 mm was used. Spectra were detected using a Synapse CCD detector (1024 pixels) thermoelectrically cooled to −60°C. Before spectra collection, the instrument was calibrated using the Rayleigh line at 0 cm^{-1} and a standard Si (100) reference band at 520.7 cm^{-1}. Samples were deposited onto Si (100) wafers, inserted into a Linkam LTS350 stage and the temperature profile modulated using a Linkam TMS94 temperature controller. The measurements were recorded in 25°C intervals, from room temperature up to 350°C in air. The heating rate was 10°C min^{-1}, with 5 min dwell time for each step to record the spectra.

3. Results and discussion

To understand the difference in chemical state between WO_3 and $W_{18}O_{49}$, we acquired the XPS results, and the high-resolution W4f and O1 s XPS spectra in both samples are shown in figure 1. For the WO_3 nanoparticle (figure 1*a*), W4f containing only W^{6+} was presented which consisted of double peaks at binding energies of 35.5 and 37.6 eV for $W4f_{7/2}$ and $W4f_{5/2}$, respectively. in the case of $W_{18}O_{49}$, the W4f core-level spectrum was broadened which indicates the multiple peak overlap, as shown in figure 1*c*. The separated two double peaks were associated with two different oxidation states of W atoms. The main peaks of $W4f_{7/2}$ (36 eV) and $W4f_{5/2}$ (38 eV) were attributed to the W^{6+} oxidation state. Another double with a lower binding energy at 34.6 and 36.8 eV was possibly caused by the emission of $W4f_{7/2}$ and $W4f_{5/2}$, respectively, and was assigned to the W^{5+} oxidation state. These results agreed well with previous reports [22–24]. The high-resolution O1s of both samples consisted of two peaks at 530.2 and 532.7 eV for the WO_3 and at 530.8 and 532.4 eV for $W_{18}O_{49}$ which could be assigned to the oxygen bond with W in the structure, respectively, as shown in figure 1*b*,*d*. The shift at 532.4 O1s of $W_{18}O_{49}$ was indicative of more defects (oxygen vacancy) and weaker W–O bounding; however, the peak at 530.8 shifted towards higher binding energy compared with the WO_3 O1s, which should be considered as evidence of the W^{5+} state inside the structure of $W_{18}O_{49}$.

At room temperature, the XRD patterns of the as-purchased WO_3 nanoparticle showed several main diffraction peaks at 23.1°, 23.6°, 24.3°, 26.6°, 28.8°, 33.4° and 34.1°, which were assigned to the (002), (020), (200), (120), (112), (022) and (202) planes of the monoclinic I (γ-WO_3) phase (COD 2106382),

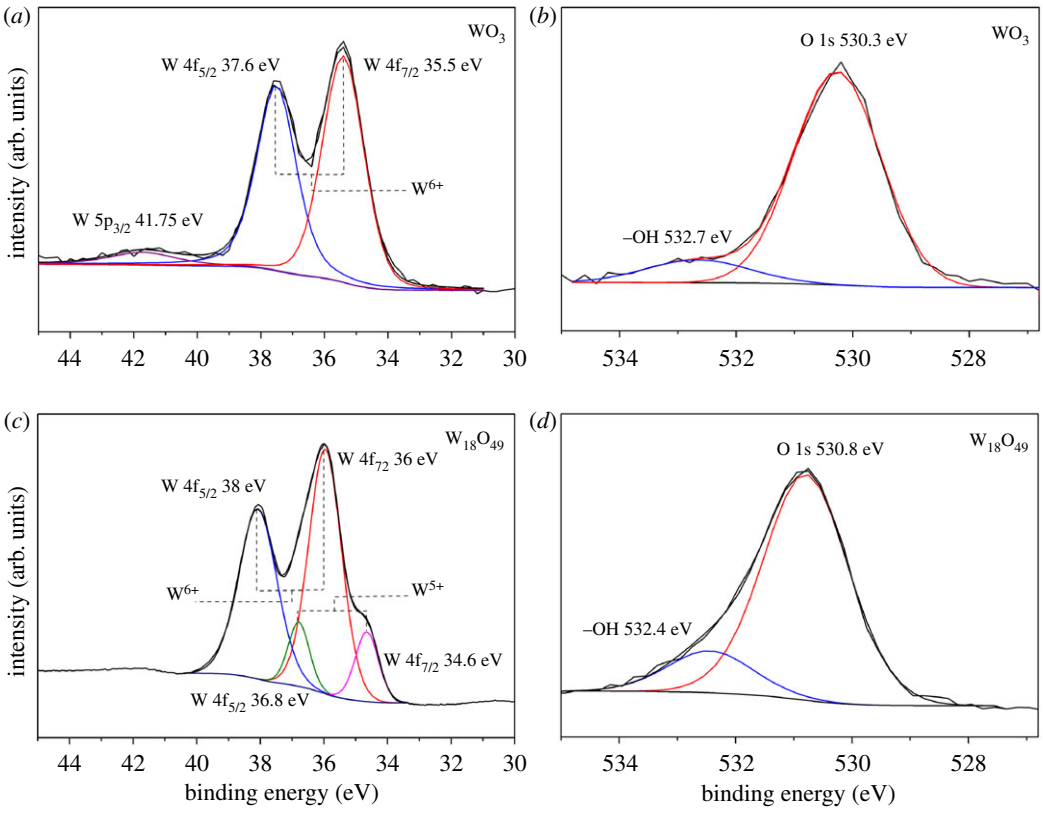

Figure 1. High-resolution XPS W4f and 01s spectra of WO_3 nanoparticles (*a*,*b*) and the as-prepared $W_{18}O_{49}$ bundled nanowires (*c*,*d*) obtained at room temperature.

respectively, as shown in figure 2*a*. These nanoparticles remained as the monoclinic phase until 250°C, with the orthorhombic phase (β-WO_3, COD 2107312) detected as the temperature reached 300°C. The main 2θ diffraction peaks appearing at 22.9°, 23.5°, 24.2°, 26.5°, 28.6°, 33.1°, 33.6° and 34.0° were indexed as the (002), (200), (020), (210), (112), (202), (022) and (220) planes, respectively. The β-WO_3 phase was continually identified until 700°C, then began to change to tetragonal α-WO_3 at 750°C. As can be seen from the XRD profile (figure 2*a*), the (202) peak started to merge with the (022) peak at approximately 24° and the (200) peak also started to merge with (020) peak at approximately 33° when the temperature reached 750°C. At 800°C, the WO_3 was completely converted to the tetragonal phase (α-WO_3, COD 1521532), with recognized peaks at 22.6°, 23.8°, 28.3°, 33.0° and 33.9° indexed as the (002), (110), (102), (112) and (200) planes of α-WO_3. The results of the cooling process, step by step from 900°C to room temperature at 50°C intervals as illustrated in figure 1*b*, clearly show that the WO_3 sample was completely transferred from α-WO_3 to β-WO_3 phase at 700°C, and from β-WO_3 to γ-WO_3 at 150°C. A mild shift of transition temperature has been recognized which could be due to the over cooling effect.

The as-prepared $W_{18}O_{49}$ nanowires exhibited typical diffraction peaks at 23.5°, 26.2°, 28.1° and 43.6° at room temperature, which were indexed to the (010), (104), (004) and (413) planes of the monoclinic γ-$W_{18}O_{49}$ phase (COD 1528166) (figure 3*a*). This phase appeared to be stable up to 500°C and then some small shoulder peaks emerged in the diffractogram, which matched well with the orthorhombic β-WO_3 phase at 550°C (COD 2107312). The main diffraction peaks at 22.9°, 23.5°, 24.2°, 26.5°, 28.6°, 33.1°, 33.6° and 34.0° were identified as the (002), (200), (020), (210), (112), (202), (022) and (220) planes of the orthorhombic phase, respectively. The orthorhombic phase remained stable until 700°C and then started to change to the α-WO_3 tetragonal phase at 750°C. As shown in figure 3*a*, the 33.1° peak (202) started to merge with the 33.6° peak (022), and the 23.5° peak (200) started to merge with the 24.2° peak (020), when the temperature reached 750°C. At 800°C, peaks at 22.6°, 23.8°, 28.3°, 33.0° and 33.9° were identified as the (002), (110), (102), (112) and (200) planes of the α-WO_3 tetragonal phase (COD 1521532), indicating the complete phase transition.

For the reverse cooling process, we have noted two key phase transitions based on the series of XRD profiles: from α-WO_3 to β-WO_3 at 800°C and β-WO_3 to γ-WO_3 at 200°C, as shown in figure 3*b*. However,

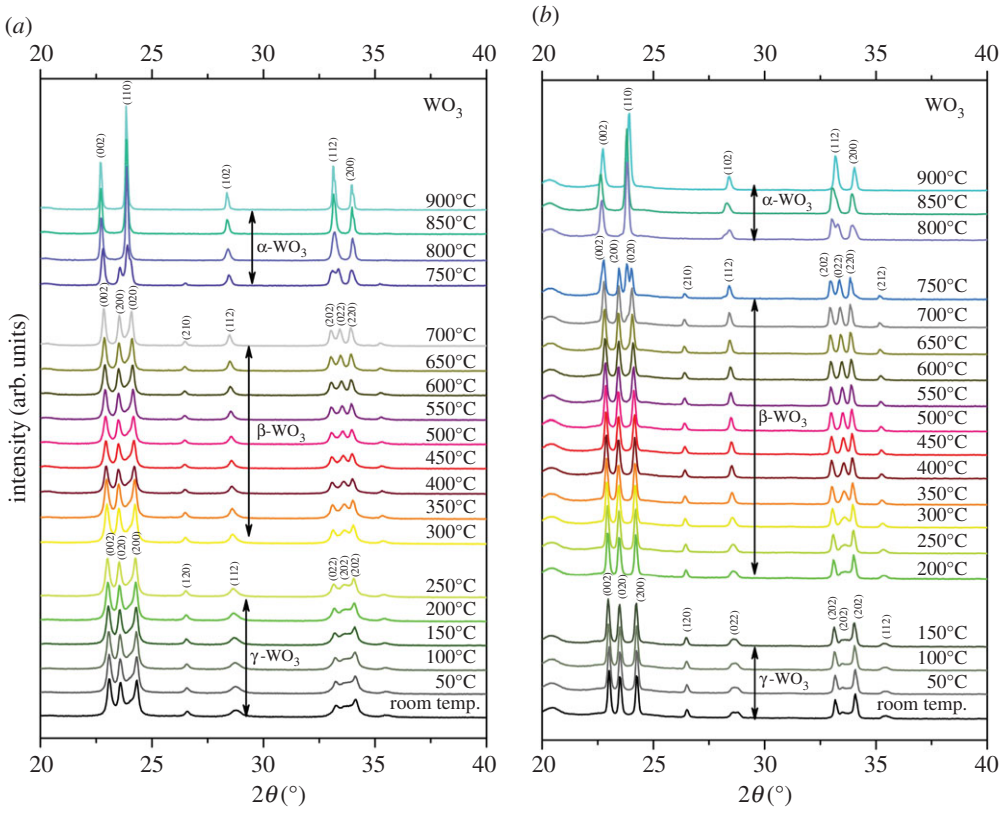

Figure 2. A series of *in situ* XRD profiles of the WO_3 nanoparticles obtained during heating (*a*) and cooling (*b*), from room temperature to 900°C, in 50°C increments.

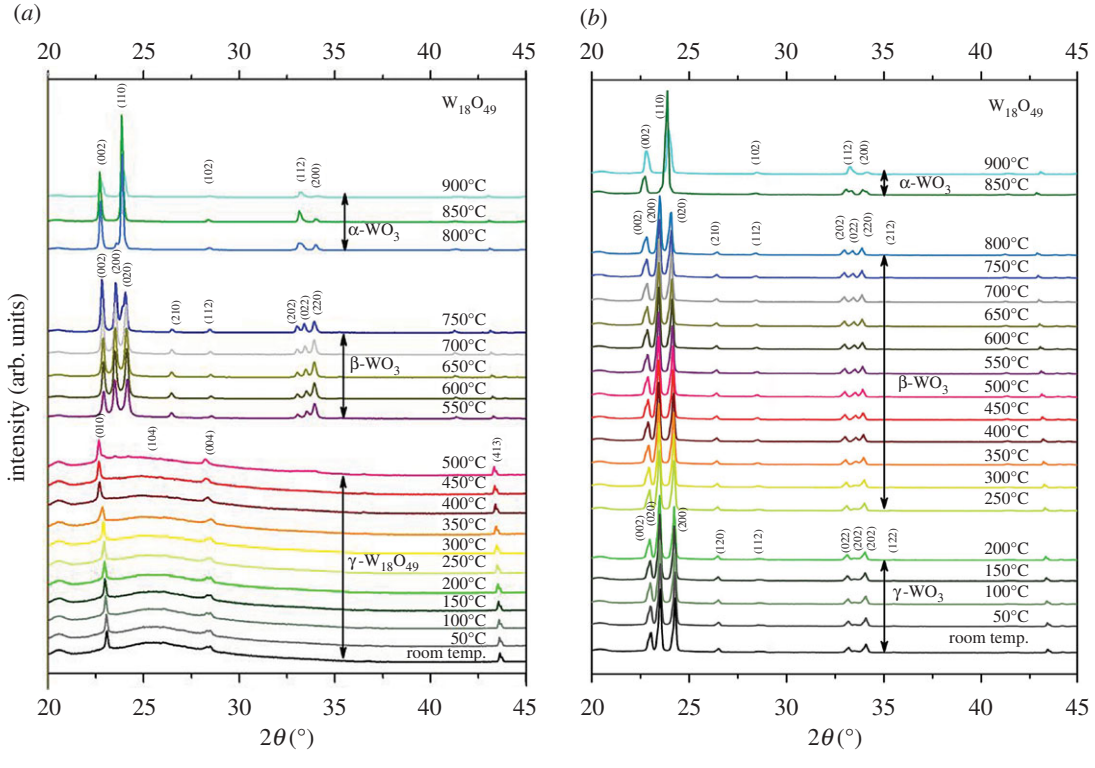

Figure 3. A series of *in situ* XRD profiles of the $W_{18}O_{49}$ nanowires obtained during heating (*a*) and cooling (*b*), from room temperature to 900°C, in 50°C increments.

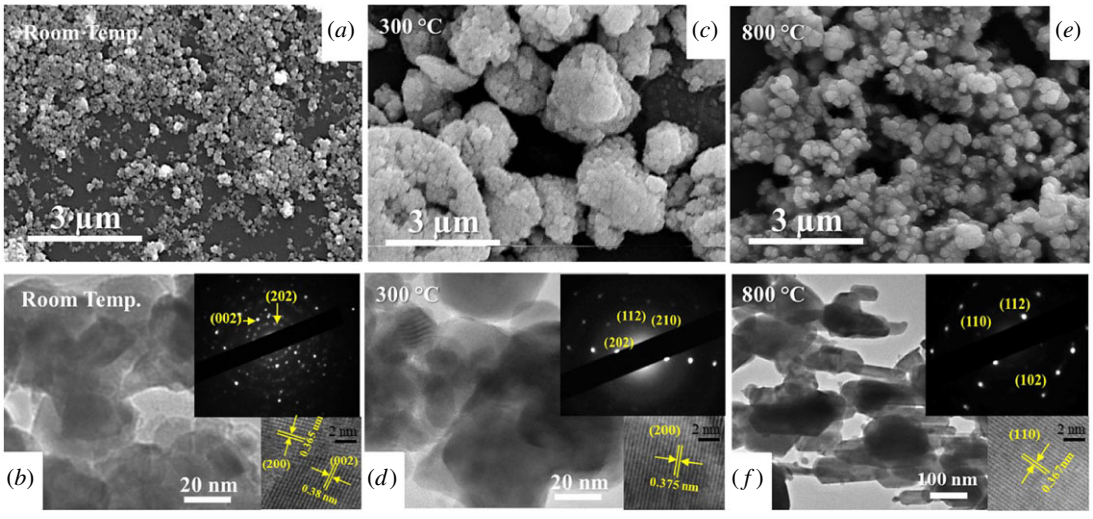

Figure 4. *Ex situ* SEM and HRTEM images of the WO_3 nanoparticles after treatment at various temperatures: (*a*,*b*) room temperature, (*c*,*d*) 300°C and (*e*,*f*) 800°C. The insets show the diffraction patterns and lattice fringe images of the monoclinic (γ), orthorhombic (β) and tetragonal (α) phases of WO_3.

the cooling process was more complicated than the heating stage, as we know that during heating the $W_{18}O_{49}$ nanowires are stable only up to 450°C, and that they will be fully oxidized, due to the minute residue oxygen in the low vacuum, to form β-WO_3 at 500°C and transition to different phases until 900°C, as described earlier. Therefore, the cooling phase of the materials cannot be reversed back to $W_{18}O_{49}$ in composition even at room temperature. Furthermore, there would be some irreversible morphological changes upon heating at higher temperatures, which will be discussed later.

Our *in situ* XRD result of the WO_3 nanoparticles was analogous to that reported by both Boulova & Lucazeau [25] and Lu *et al*. [18] in the lower temperature range, which was that the γ-WO_3 phase started to transition to the β-WO_3 phase at about 250°C. However, the α-WO_3 phase transformation at about 670°C reported by them occurred at about 750°C in our case, which is much closer to the transition temperature of bulk WO_3 structure [11]. Furthermore, we could not identify the triclinic (δ-WO_3) and hexagonal (h-WO_3) phases during our investigation. For the $W_{18}O_{49}$ nanowires, the present results further confirmed the previous *ex situ* study conducted by Sun *et al*. [19] that found the monoclinic γ-$W_{18}O_{49}$ only remained stable at temperatures below 450°C and completely transformed to the monoclinic β-WO_3 phase above 500°C. However, these converted WO_3 nanoparticles remained stable up to 900°C without further crystalline transitions based on the XRD results, which was slightly different from the original WO_3 nanoparticles (lower by about 50°C than the nanowires). The result might be due to the difference in geometry and crystalline structures between the $W_{18}O_{49}$-converted WO_3 and the as-received WO_3, because the transformation from $W_{18}O_{49}$ to WO_3 would inevitably involve crystal lattice rearrangement via atomic diffusion which will subsequently exaggerate the morphology evolution and oxygen vacancy filling [26]. WO_3 presented the reversible phase transitions at lower temperature during cooling, compared with the heating process, whereas the $W_{18}O_{49}$ did not show any phase transition at low temperature (below 500°C), only existed as monoclinic, and did not exhibit reversible phase changes during cooling down from high temperature at 900°C (remained as WO_3).

The SEM and high-resolution TEM images both confirmed the morphological changes and phase transitions of the two materials, as shown in figures 4 and 5. The average size of the original monoclinic WO_3 nanoparticle was about 40 nm in diameter (figure 4*a*), which appeared to be larger and severely agglomerated after the 300°C heating treatment (figure 4*c*). The nanoparticles were also no longer in the monoclinic γ-phase, having been converted to orthorhombic β-WO_3. As the temperature was raised above 800°C further changes to both the crystal phase and morphology were observed, with tetragonal α-WO_3 nanorods possessing diameters around 100–150 nm afforded. The HRTEM lattice fringes and the selected area diffraction patterns of each phase shown (figure 4, insets) matched very well with our XRD results.

The SEM images of the as-prepared $W_{18}O_{49}$ nanowires indicated average dimensions of approximately 3 µm in length and 50 nm in diameter. TEM analysis further confirmed that the as-prepared $W_{18}O_{49}$ nanowires consisted of ultrathin nanowires of only approximately 2–5 nm in diameter

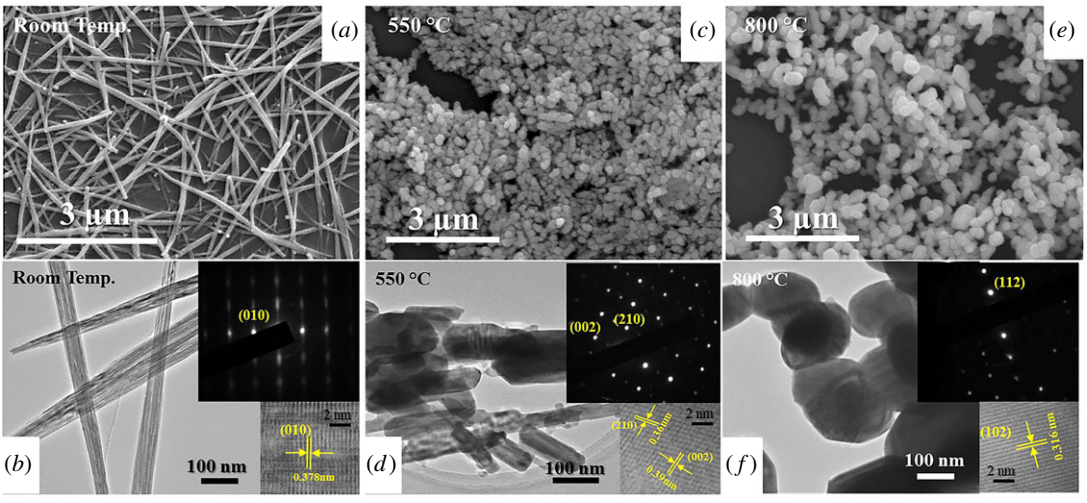

Figure 5. SEM and HRTEM images of the bundled $W_{18}O_{49}$ nanowires at room temperature (*a*,*b*), 550 (*c*,*d*) and 800°C (*e*,*f*), which were identified as the monoclinic γ-$W_{18}O_{49}$, orthorhombic β-WO_3 and tetragonal α-WO_3 phases, respectively.

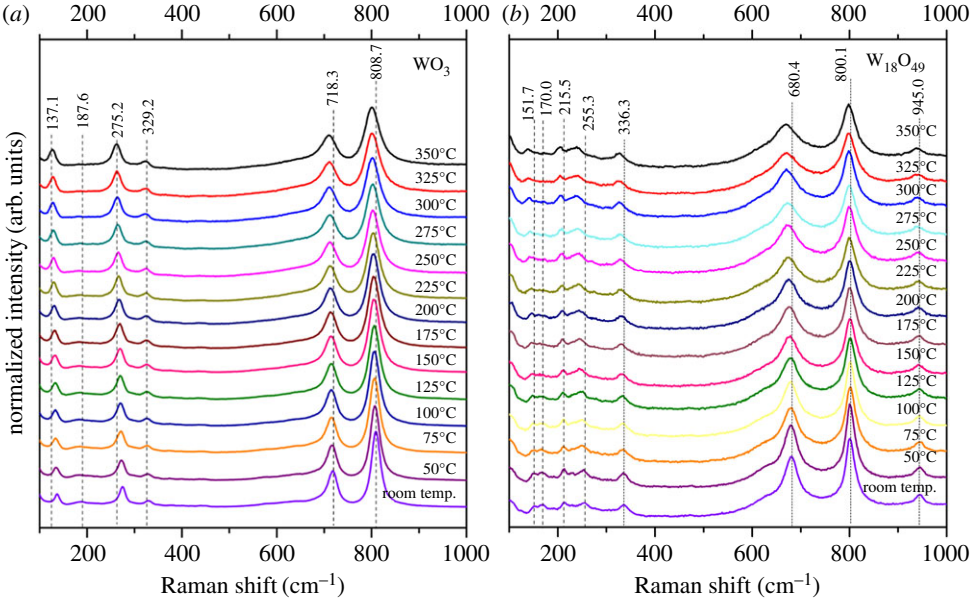

Figure 6. Raman spectra of the WO_3 nanoparticles (*a*) and bundled $W_{18}O_{49}$ nanowires (*b*), under different annealing temperatures ranging from room temperature up to 350°C, increasing at 25°C for each stage, acquired with 1% laser power (0.336 mW).

and up to 2 µm in length, self-assembled into bundles [19], hence the larger apparent diameter under SEM was owing to the lower resolution. In figure 5*b*, the streaking feature noted in the SAED pattern and the parallel HRTEM lattice fringes of the $W_{18}O_{49}$ nanowires both clearly demonstrated the bundled nature of the individual nanowires and that nanowires within a bundle were grown along the same direction of ⟨010⟩. The easily recognizable (010) plane spacing was approximately 0.378 nm, in good agreement with the XRD result of the monoclinic $W_{18}O_{49}$. After the 550°C treatment (figure 5*d*), short nanobricks, with a diameter of about 100 nm and length up to 200 nm, of WO_3 were observed, which were subsequently converted into larger particles of about 200 nm in diameter after treatment at 800°C (figure 5*f*). The SAED and HRTEM results also showed that both the 550 and 800°C treated samples matched well with our XRD results. The ultrathin $W_{18}O_{49}$ sub-stoichiometric nanowires were only stable up to 500°C, then began to oxidize and were completely converted to the orthorhombic phase of WO_3 at 550°C, due to the presence of minute residue oxygen in the low vacuum. Furthermore, the blue thin film

Table 1. The Raman shifts of WO_3 and $W_{18}O_{49}$ in the range 100–1000 cm^{-1}. υ, stretching; δ, deformation/in-plane bending.

		band positions (cm^{-1})						
		peak 1	peak 2	peak 3	peak 4	peak 5	peak 6	peak 7
	temperature (°C)	lattice modes		δ (O–W–O)		υ (O–W–O)		υ (W=O)
WO_3 nanoparticles	room temp.	137.1	187.6	275.2	329.2	718.3	808.7	—
	50	134.7	184.8	272.5	327.6	716.6	807	—
	75	134.2	183.2	272.2	326.9	715.6	806.4	—
	100	133.5	184.9	270.0	325.6	714.9	805.8	—
	125	133.3	184.1	269.5	325.8	714.3	805.3	—
	150	132.6	183.9	269.3	325.5	714.1	804.9	—
	175	131.3	183.0	269.5	325.1	713.8	804.9	—
	200	131.3	184.2	266.9	325.1	713	803.8	—
	225	129.8	186.8	266.2	325.3	712.6	802.5	—
	250	129.1	181.8	265.6	324.6	711.8	802.5	—
	275	129.0	—	265.0	323.4	712.1	802.9	—
	300	127.9	—	263.6	323.5	710.6	801.8	—
	325	128.7	—	262.6	323.4	711	800.2	—
	350	127.1	—	262.1	322.6	709.8	800	—
	reverse at room temp.	129.3	181.4	267.3	322.3	711.8	802.3	—
bundle $W_{18}O_{49}$ nanowires	room temp.	151.7	170.0	255.3	336.3	680.4	800.1	945.0
	50	150.1	166.4	253.5	334.5	678.7	800.1	945.0
	75	153.6	166.4	248.1	334.5	680.4	801.8	948.3
	100	148.1	170.0	248.1	334.5	680.4	801.8	945.0
	125	148.1	170.0	246.3	332.7	678.7	800.1	943.3
	150	151.7	—	244.5	329.1	678.7	801.8	941.6
	175	146.3	—	244.5	330.9	675.3	801.8	945.0
	200	146.5	—	244.5	332.7	675.3	801.8	941.6
	225	146.3	—	240.9	330.9	675.3	798.4	943.3
	250	140.8	—	244.5	329.1	670.1	798.4	941.6
	275	144.4	—	239.1	325.5	671.8	800.1	938.3
	300	142.6	—	235.4	325.5	670.1	798.4	940.0
	325	138.9	—	240.7	325.5	671.8	798.4	936.6
	350	138.9	—	239.1	327.3	670.1	798.4	938.3
	reverse at room temp.	144.4	—	246.3	327.3	673.6	795.1	938.3

turned to yellow during this stage. Meanwhile, the long and thin bundles were broken and reassembled into short and fat nanorods and eventually became much larger particles.

While the above analytical techniques are extremely helpful in analysing the crystalline and morphological features, *in situ* Raman spectroscopy can provide more insight into the bonding within the two nanomaterials under examination. The *in situ* Raman spectra of the WO_3 nanoparticles and the bundled $W_{18}O_{49}$ nanowires from room temperature up to 350°C (due to the limitation of the heating stage) were shown together in figure 5, for comparison. At room temperature, the structure of the monoclinic WO_3 crystal consisted of corner-shared octahedral with the W atoms displaced from the centres, to form zigzag chains with alternating short and long W–O bond lengths. In figure 6*a*, the bands at 718 and 809 cm^{-1} were assigned to O–W–O stretches, associated with longer (1.88 Å) and shorter (1.82 Å) W–O bonds, respectively. The bands at 275 and 329 cm^{-1} were attributed to the O–W–O bending and O–W–O deformation modes, respectively. The other two peaks located at 137.1 and

187.5 cm^{-1} belonged to the lattice vibration modes, consistent with previous studies [27]. The structure of $W_{18}O_{49}$ could be derived from that of WO_3 by introducing oxygen vacancies compensated by a pair of pentagonal columns of edge-sharing octahedral to produce hexagonal channels which run through the structure. This complex structure was expected to contain a range of O–W–O bond lengths which resulted in a broadening of the bands. The Raman spectra of the bundled $W_{18}O_{49}$ nanowires (figure 6*b*) exhibited three main regions. The high wavenumber bands included two peaks at approximately 680 and 800 cm^{-1}, which could be assigned to the asymmetric and symmetric stretching vibration mode of O–W–O. The 255 cm^{-1} band was attributed to the O–W–O bending mode of bridging oxygen, and the 336 cm^{-1} band to the O–W–O deformation mode [28]. Moreover, the weak band at approximately 940 cm^{-1} could be used as the characteristic shift for $W_{18}O_{49}$ nanowires, because it did not exist in the WO_3 nanoparticles, and has been ascribed to the W=O stretching vibration mode of a terminal oxygen. Such a moiety did not exist in WO_3, but was expected to be present in the channels of sub-stoichiometric tungsten oxide species. The intensity of this peak remained constant during the heating experiment, indicating the stability of the nanowires up to 350°C. To clearly show the features of the Raman shift, we summarized the Raman peak positions in table 1. The decrease in the wavenumber of the stretching and bending modes with increasing temperature corresponded to an increase in the O–W–O bond length for both structures.

Boulova & Lucazeau [25] also studied the structural transitions of WO_3 nanoparticles (average size approx. 35 nm) by using *in situ* Raman spectroscopy, from room temperature to 677°C (950 K). They found that samples began to transform from γ-WO_3 to β-WO_3 phase at a temperature of about 500 K (227°C) and then to α-WO_3 at about 850 K (577°C). Similar phase transitions of much larger WO_3 nanowires (40–80 nm in diameter and 1 µm in length) were reported by Lu *et al*. [18] using *in situ* Raman spectroscopy, where it was reported that the γ- to β-WO_3 transition occurred at 230°C. Although these two studies did not provide the exact characteristic wavenumbers of β-WO_3, our present wavenumber downshifts with increased heating temperatures appeared to agree well with their analyses. Downshifting to lower wavenumbers in the stretching and bending shift positions was a result of increased bond lengths between the W and O in the lattice. In fact, this increase in bond length was maintained, even back to room temperature, as verified in our *ex situ* HRTEM examination that the lattice distance of the (200) plane changed from 0.365 to 0.375 nm (figure 4*b*,*d*). Taking into account our *in situ* XRD results, we understood that the transition from the γ-WO_3 to the β-WO_3 phase occurred at around 300°C for the WO_3 particles and at 550°C for the $W_{18}O_{49}$ nanowires. This γ to β transition point matched with our *in situ* Raman spectroscopy result that occurred at 275°C. Therefore, the disappearance of the 187.6 cm^{-1} band of WO_3 was believed to be the fingerprint of the transition from γ- to β-WO_3. Hence in table 1, we assigned the major stretching vibrational modes of β-WO_3 phase at 802.9 and 712.1 cm^{-1}, 323.4 and 265 cm^{-1} for the bending modes and 129 cm^{-1} for the lattice mode. For the $W_{18}O_{49}$ nanowires, we believed that they remained as the monoclinic γ-phase at 350°C, based on the two *in situ* observations; however, downshift with increase of temperature in the Raman spectra was noted. Thus, we believed that the peak shift could be an indicator of the relaxation of the channel inside the WO_3 and $W_{18}O_{49}$ structures or the elimination of the impurity inside the structures [29]. Finally, it is clear that the phase change loop of these two different structures was different, due to the combination of the original geometry and slight compositional differences of the samples.

4. Conclusion

We have demonstrated that different geometries of WO_3 nanoparticles and $W_{18}O_{49}$ nanowires exhibited different phase transition behaviours. The hot-stage XRD results have confirmed that, different from the γ-WO_3 nanoparticles that converted to β-WO_3 just below 300°C, the γ-$W_{18}O_{49}$ nanowires remained stable up to 500°C, then completely oxidized and transferred to β-WO_3 at 550°C. The *in situ* Raman spectroscopy investigations have confirmed the downshift of peak position, which has been attributed to the increased length of the W–O chemical bonds inside the lattice. We have identified the 187.6 cm^{-1} fingerprint band as a means of identifying the phase transition from γ- to β-WO_3 nanoparticle structures at 275°C, which is about 75°C lower than the relaxation temperature of above 350°C for the monoclinic γ-$W_{18}O_{49}$ nanowires. This finding suggests the better thermal stability and often higher performance of the ultrathin $W_{18}O_{49}$ nanowires compared with those of the WO_3 nanoparticles. The understanding of these fine differences in phase transition and structural stability between bundled ultrathin $W_{18}O_{49}$ nanowires and spherical WO_3 nanoparticles offers helpful guidance in the design and development of WO_x-based nanomaterials in nanodevices.

Data accessibility. This article does not contain any additional data.

Authors' contributions. K.T. carried out the *in situ* hot-stage XRD experiments and SEM and TEM observations; F.X. and G.R. carried out the XPS and *in situ* Raman investigation. All authors contributed to the interpretation of the results and drafting of the manuscript. Y.Z. is leading the project.

Competing interests. We have no competing interests.

Funding. K.T. and Y.Z. thank Qioptiq for providing some financial support for the experiments. This study was funded by the Engineering and Physical Sciences Research Council (EP/N034627/1).

References

1. Nandi DK, Sarkar SK. 2014 Atomic layer deposition of tungsten oxide for solar cell application. *Energy Procedia* **54**, 782–788. (doi:10.1016/j.egypro.2014.07.321)
2. Qin Y, Li X, Wang F, Hu M. 2011 Solvothermally synthesized tungsten oxide nanowires/nanorods for NO_2 gas sensor applications. *J. Alloys Comp.* **509**, 8401–8406. (doi:10.1016/j.jallcom.2011.05.100)
3. Pal S, Chattopadhyay KK. 2016 Tungsten oxide nanostructures for energy storage and field emission applications. *J. Eng. Technol. Res.* **5**, 97–101.
4. Wicaksana Y, Liu S, Scott J, Amal R. 2014 Tungsten trioxide as a visible light photocatalyst for volatile organic carbon removal. *Molecules* **19**, 17 747–17 762. (doi:10.3390/molecules191117747)
5. Djaoued Y, Balaji S, Brüning R. 2012 Electrochromic devices based on porous tungsten oxide thin films. *J. Nanomater.* **2012**, 1–9. (doi:10.1155/2012/674168)
6. Zhu LF, She JC, Luo JY, Deng SZ, Chen J, Ji XW, Xu NS. 2011 Self-heated hydrogen gas sensors based on Pt-coated $W_{18}O_{49}$ nanowire networks with high sensitivity, good selectivity and low power consumption. *Sens. Actua. B Chem.* **153**, 354–360. (doi:10.1016/j.snb.2010.10.047)
7. Leftheriotis G, Papaefthimiou S, Yianoulis P, Siokou A. 2001 Effect of the tungsten oxidation states in the thermal coloration and bleaching of amorphous WO_3 films. *Thin. Solid Films* **384**, 298–306. (doi:10.1016/s0040-6090(00)01828-9)
8. Shirke YM, Porel Mukherjee S. 2017 Selective synthesis of WO_3 and $W_{18}O_{49}$ nanostructures: ligand-free pH-dependent morphology-controlled self-assembly of hierarchical architectures from 1D nanostructure and sunlight-driven photocatalytic degradation. *Cryst. Eng. Comm.* **19**, 2096–2105. (doi:10.1039/c6ce02518h)
9. Frey GL, Rothschild A, Sloan J, Rosentsveig R, Popovitz-Biro R, Tenne R. 2001 Investigations of nonstoichiometric tungsten oxide nanoparticles. *J. Solid State Chem.* **162**, 300–314. (doi:10.1006/jssc.2001.9319)
10. Zheng H, Ou JZ, Strano MS, Kaner RB, Mitchell A, Kalantar-zadeh K. 2011 Nanostructured tungsten Oxide—properties, synthesis, and applications. *Adv. Funct. Mater.* **21**, 2175–2196. (doi:10.1002/adfm.201002477)
11. Woodward PM, Sleight AW, Vogt T. 1997 Ferroelectric tungsten trioxide. *J. Solid State Chem.* **131**, 9–17. (doi:10.1006/jssc.1997.7268)
12. Gubbala S, Thangala J, Sunkara MK. 2007 Nanowire-based electrochromic devices. *Sol. Energy Mater. Sol. Cells.* **91**, 813–820. (doi:10.1016/j.solmat.2007.01.01)
13. Rawal SB, Bera S, Lee WI. 2012 Visible-light photocatalytic properties of $W_{18}O_{49}/TiO_2$ and WO_3/TiO_2 heterocomposites. *Catal. Lett.* **142**, 1482–1488. (doi:10.1007/s10562-012-0924-z)
14. Zhu YQ, Hu W, Hsu WK, Terrones M, Grobert N, Hare JP, Terrones H. 1999 Tungsten oxide tree-like structures. *Chem. Phys. Lett.* **309**, 327–334. (doi:10.1016/s0009-2614(99)00732-0)
15. Chen J, Chen S, Lu D, Zhang W, Xie F, Xie W, Wang C. 2010 Pressure-Induced Structural Transition in WO_3 Nanowires. *Chem. Phys. Chem.* **11**, 2546–2549. (doi:10.1002/cphc.201000341)
16. Cazzanelli E. 1999 Raman study of the phase transitions sequence in pure WO_3 at high temperature and in H_xWO_3 with variable hydrogen content. *Solid State Ionics* **123**, 67–74. (doi:10.1016/s0167-2738(99)00101-0)
17. Lai CW. 2015 Surface morphology and growth of anodic titania nanotubes films: photoelectrochemical water splitting studies. *J. Nanomater.* **2015**, 1–7. (doi:10.1155/2015/820764)
18. Lu DY, Chen J, Zhou J, Deng SZ, Xu NS, Xu JB. 2007 Raman spectroscopic study of oxidation and phase transition in $W_{18}O_{49}$ nanowires. *J. Raman Spectrosc.* **38**, 176–180. (doi:10.1002/jrs.1620)
19. Sun S, Zhao Y, Xia Y, Zou Z, Min G, Zhu Y. 2008 Bundled tungsten oxide nanowires under thermal processing. *Nanotechnology.* **19**, 305709. (doi:10.1088/0957-4484/19/30/305709)
20. Liu JX, Dong XL, Liu XW, Shi F, Yin S, Sato T. 2011 Solvothermal synthesis and characterization of tungsten oxides with controllable morphology and crystal phase. *J. Alloys Compounds* **509**, 1482–1488. (doi:10.1016/j.jallcom.2010.10.052)
21. Thummavichai K, Trimby L, Wang N, Wright CD, Xia YD. 2017 Low temperature annealing improves the electrochromic and degradation behavior of tungsten oxide (WO_x) thin films. *J. Phys. Chem. C* **121**, 20 498–20 506. (doi:10.1021/acs.jpcc.7b06300)
22. Baek Y, Yong K. 2007 Controlled growth and characterization of tungsten oxide nanowires using thermal evaporation of WO_3 powder. *J. Phys. Chem. C* **111**, 1213–1218. (doi:10.1021/jp0659857)
23. Saleem M, Al-Kuhaili MF, Durrani SMA, Hendi AHY, Bakhtiari IA, Ali S. 2015 Influence of hydrogen annealing on the optoelectronic properties of WO_3 thin films. *Int. J. Hydrog. Energy* **40**, 12 343–12 351. (doi:10.1016/j.ijhydene.2015.06.078)
24. Guo C, Yin S, Yan M, Kobayashi M, Kakihana M, Sato T. 2012 Morphology-controlled synthesis of $W_{18}O_{49}$ nanostructures and their near-infrared absorption properties. *Inorg. Chem.* **51**, 4763–4771. (doi:10.1021/ic300049j)
25. Boulova M, Lucazeau G. 2002 Crystallite nanosize effect on the structural transitions of WO_3 studied by raman spectroscopy. *J. Solid State Chem.* **167**, 425–434. (doi:10.1006/jssc.2002.9649)
26. Cho MH, Park SA, Yang KD, Lyo IW, Jeong K, Kang SK, Shin HJ. 2004 Evolution of tungsten-oxide whiskers synthesized by a rapid thermal-annealing treatment. *J. Vac. Sci. Technol. B* **22**, 1084–1087. (doi:10.1116/1.1738670)
27. Rajagopal S, Nataraj D, Mangalaraj D, Djaoued Y, Robichaud J, Khyzhun OY. 2009 Controlled growth of WO_3 nanostructures with three different morphologies and their structural, optical, and photodecomposition studies. *Nanoscale Res. Lett.* **4**, 1335–1342. (doi:10.1007/s11671-009-9402-y)
28. Ma Z, Weng D, Wu X, Si Z. 2012 Effects of WOx modification on the activity, adsorption and redox properties of CeO_2 catalyst for NO_x reduction with ammonia. *J. Environ. Sci.* **24**, 1305–1316. (doi:10.1016/s1001-0742(11)60925-x)
29. Vijayalakshmi K, Pillay VV. 2011 Effect of heat treatment on the NO_2-sensing properties of sputter-deposited indium tin oxide thin films. *Philos. Mag. Lett.* **91**, 682–689. (doi:10.1080/09500839.2011.608731)